npj | 2d materials and applications

Article

Published in partnership with FCT NOVA with the support of E-MRS

https://doi.org/10.1038/s41699-024-00449-w

Electric field tunable bandgap in twisted double trilayer graphene

Check for updates

Mickael L. Perrin [1,2,3] ✉, Anooja Jayaraj [4], Bhaskar Ghawri [1], Kenji Watanabe [5], Takashi Taniguchi [6], Daniele Passerone [4], Michel Calame [1,7,8] ✉ & Jian Zhang [1] ✉

Twisted van der Waals heterostructures have recently emerged as a versatile platform for engineering interaction-driven, topological phenomena with a high degree of control and tunability. Since the initial discovery of correlated phases in twisted bilayer graphene, a wide range of moiré materials have emerged with fascinating electronic properties. While the field of twistronics has rapidly evolved and now includes a range of multi-layered systems, moiré systems comprised of double trilayer graphene remain elusive. Here, we report electrical transport measurements combined with tight-binding calculations in twisted double trilayer graphene (TDTLG). We demonstrate that small-angle TDTLG (~1.7−2.0°) exhibits an intrinsic bandgap at the charge neutrality point. Moreover, by tuning the displacement field, we observe a continuous insulator-semimetal-insulator transition at the CNP, which is also captured by tight-binding calculations. These results establish TDTLG systems as a highly tunable platform for further exploration of magneto-transport and optoelectronic properties.

The ability to tune the twist angle between different layers of two-dimensional materials has led to a paradigm shift in quantum band engineering. The low-energy electronic structure of twisted heterostructure is determined by the moiré potential originating from the rotational misalignment of the constituent layers. Alternatively, superlattices can also be realized based on the mismatch between the lattice constants of these layers. After the initial discovery of correlated insulating states[1] and superconductivity[2] in twisted bilayer graphene, the field of twistronics has expanded to various moiré systems, such as ABC-stacked trilayer graphene (TLG) with hexagonal boron nitride (TLG/h-BN)[3,4], twisted double bilayer graphene (TDBLG)[5–7], twisted monolayer-bilayer graphene[8,9], twisted trilayer graphene[10,11], twisted tetralayer and pentalayer graphene[12], and transition metal dichalcogenide (TMD) heterostructures[13,14]. A plethora of broken-symmetry phases, including but not limited to correlated insulators[1,5], superconductivity[2,10,15] quantum anomalous Hall effect[16], ferromagnetism[8,17,18], strange metal[19,20], and Wigner crystals[21,22] have been discovered in various moiré systems.

Twisted double trilayer graphene (TDTLG), which has only scarcely been explored to date, is a natural extension of the world of moiré materials. In particular, TDTLG fabricated with two ABC-stacked TLG layers (Fig. 1a, b) provides an appealing platform to tune the band structure of the hybrid system as single ABC-stacked TLG features van Hove singularities at or near the band edge where the density of states (DOS) diverges[23]. Moreover, the recent observation of ferromagnetism[24] and superconductivity[25] in moiréless ABC-stacked TLG make it a natural choice for exploring ABC-stacked TDTLG systems. Although the unconventional lattice relaxation effects in TDTLG have been explored using nano-optical and tunneling spectroscopic tools[26], transport experiments at low twist angles remain elusive. In this work, we have performed electric transport measurements in small-angle TDTLG (~1.7−2.0°), where we demonstrate the exceptional tunability of the band structure in the presence of an external electric field. In particular, we find a continuous transition from an insulating state to a semimetallic state and again to an insulating state with an increasing displacement field. We refer to this transition as the insulator-semimetal-insulator hereafter in the text.

Results and discussion

Device fabrication

The trilayer graphene flakes were obtained via mechanical exfoliation of graphite crystals and the TDTLG devices were fabricated using the tear-and-

[1]Transport at Nanoscale Interfaces Laboratory, Empa, Swiss Federal Laboratories for Materials Science and Technology, 8600 Dübendorf, Switzerland. [2]Department of Information Technology and Electrical Engineering, ETH Zurich, 8092 Zurich, Switzerland. [3]Quantum Center, ETH Zürich, 8093 Zürich, Switzerland. [4]nanotech@surfaces Laboratory, Empa, Swiss Federal Laboratories for Materials Science and Technology, 8600 Dübendorf, Switzerland. [5]Research Center for Functional Materials, National Institute for Materials Science, 1-1 Namiki, Tsukuba 305-0044, Japan. [6]International Center for Materials Nanoarchitectonics, National Institute for Materials Science, 1-1 Namiki, Tsukuba 305-0044, Japan. [7]Department of Physics, University of Basel, 4056 Basel, Switzerland. [8]Swiss Nanoscience Institute, University of Basel, 4056 Basel, Switzerland. ✉e-mail: mickael.perrin@empa.ch; michel.calame@empa.ch; jian.zhang@empa.ch

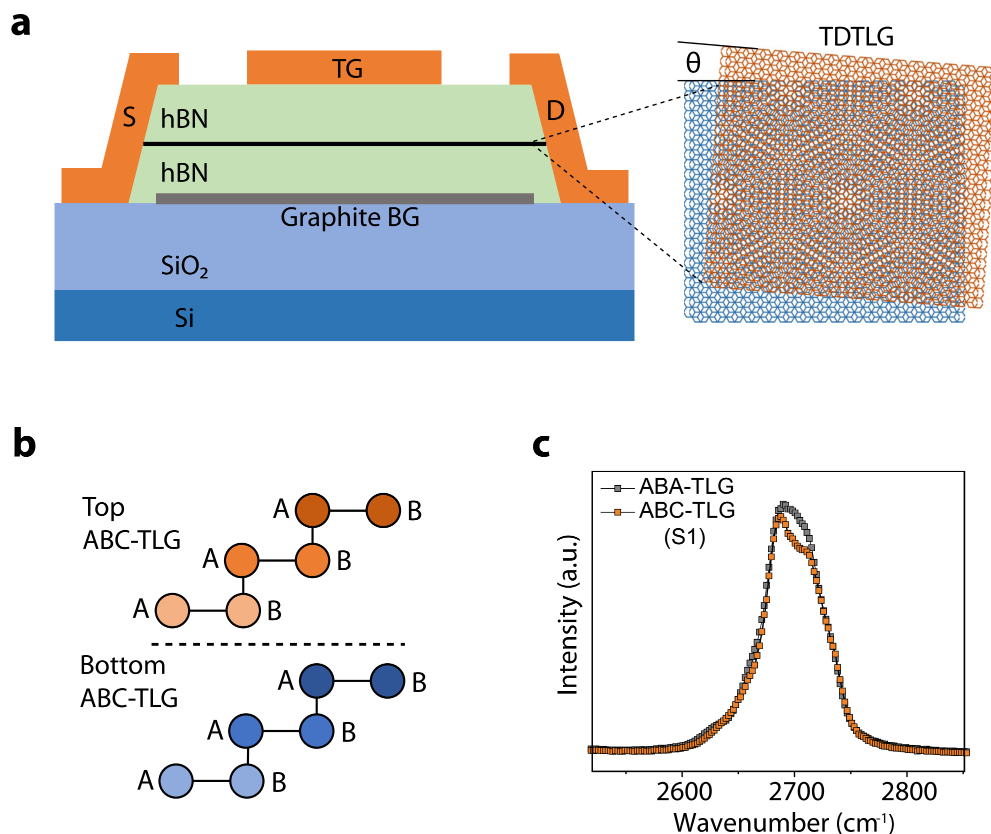

Fig. 1 | Device structure. a Schematic cross-sectional view of the device, showing the constituent layers, electrical contacts, and the gate assembly. The Au bar and graphite layer serve as top (TG) and bottom (BG) gates, respectively. The zoomed-in region shows the TDTLG moiré superlattice. **b** Schematic illustration of the atomic configuration of TDTLG layers, with ABC-stacking order as representative. **c** Comparison between Raman spectra obtained from ABA and ABC TLG flakes.

stack dry-transfer method[27,28] (see Methods for the detailed fabrication process). The layer thickness was identified by optical microscopy and confirmed by Raman spectroscopy prior to the device fabrication (Supplementary Fig. 1). The stacking order for the TLG flakes is also determined by Raman spectroscopy, where the 2D peak of the TLG is found to be more asymmetric, with a pronounced shoulder. This indicates an ABC-stacking order at the measured points (Supplementary Fig. 1). A comparison of Raman spectra between an ABC- and an ABA-stacked TLG is shown in Fig. 1c. It should be noted that, although the intended stacking was ABC-ABC, the relaxation process during the transfer and device fabrication can result in alternate stacking configurations, as discussed later. Four dual-gated TDTLG devices with different twist angles θ of $1.8 \pm 0.015^{\circ}$ (S1), $1.69 \pm 0.003^{\circ}$ (S2), $2.0 \pm 0.022^{\circ}$ (S3), and $1.96 \pm 0.02^{\circ}$ (S4) were measured to reveal the transport behavior in TDTLG. Figure 1a presents a schematic illustration of our h-BN encapsulated dual-gated TDTLG device. The TDTLG is contacted through 1D edge contacts with Cr/Au electrodes. A top metal electrode is deposited to form a dual-gate device, where the TDTLG can be gated by both the top metal gate and the bottom graphite gate. This dual-gate configuration allowed us to independently tune the carrier density (n) of the TDTLG and vertical displacement field (D) across the heterostructure. D and n are given by, $D/\epsilon_0 = [C_{BG}(V_{BG} - V_{B0}) - C_{TG}(V_{TG} - V_{T0})]/2$ and $n = [(C_{BG}(V_{BG} - V_{B0}) + C_{TG}(V_{TG} - V_{T0})]/e$, where C_{BG} and C_{TG} are the unit area bottom and top gate geometric capacitances, respectively, and V_{B0} and V_{T0} are the gate voltages corresponding to the intrinsic doping. We note that the top gate does not cover the entire channel (see Fig. 1a). As a result, in part of the channel, n and D cannot be controlled.

Electric field tunable bandgap

Figure 2a shows the resistance R measured in device S1 with $\theta = 1.8^{\circ}$ as a function of V_{TG} and V_{BG}. The phase space exhibits multiple resistive features in the entire range of V_{TG} and V_{BG}. The central diagonal resistance line corresponds to the charge neutrality point (CNP_{DG}) of the dual-gated TDTLG region, which is underneath the top gate. In contrast, the two diagonal resistance lines at the top-right and bottom-left correspond to the full filling of the moiré superlattice bands ($\pm n_s$), which allows us to calculate the twist angle (see Methods). We also observe three additional, horizontal, resistive features, which we identify as the CNP and the superlattice peaks of the singly-gated regions of the sample, which are not affected by the top gate. The different peaks become more apparent when plotting a line cut of R as a function of n at $D/\epsilon_0 = 0$, as shown in Fig. 2b.

Further, to understand the effect of the displacement field on the band structure of TDTLG, we show a high-resolution resistance map (separate measurement from Fig. 2a) as a function of n and D field in Fig. 2c. We find that TDTLG shows an intrinsic bandgap in the absence of a displacement field. The absence of a bandgap at zero field in the underlying TLG suggests that the gap emerges due to the intrinsic superlattice structure. However, when a displacement field is applied in either direction, the gap gradually fades out and disappears at a finite field, indicating an insulator-to-semimetal phase transition in this region. More strikingly, when the D is increased further, the gap opens again with increasing width.

To better visualize the evolution of the bandgap as a function of the displacement field, we plot R as a function of D at $n = 0$ in Fig. 2d. Here, an insulator-semimetal transition is observed at around $D/\epsilon_0 = 0 \pm 0.1$ V/nm and a semimetal-insulator transition at around $D/\epsilon_0 = \pm 0.2 \pm 0.3$ V/nm. In contrast, the resistive peaks at $\pm n_s$ show an insulating behavior in the investigated range of D. Based on these experimental observations, we schematically show the expected low-energy band structure of TDTLG at three different values of D (Fig. 2e). The figure shows a bandgap that is finite at $D/\epsilon_0 = 0$, closes at $D = D_0$, where $D_0/\epsilon_0 \sim 0.1$ V/nm, and then opens again for $D > D_0$. We note that all three devices show similar characteristics with

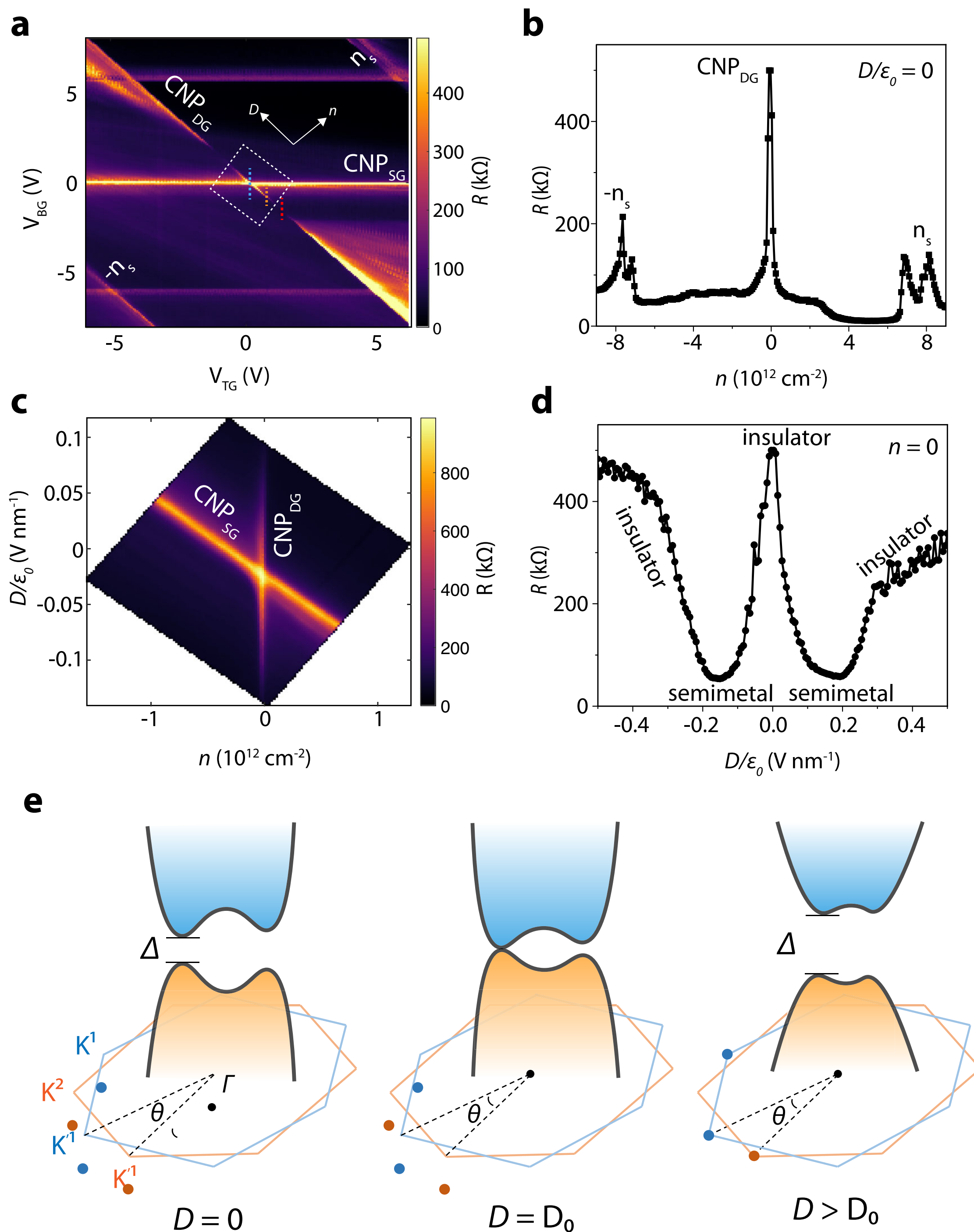

Fig. 2 | Electrical characterization. a Two-probe resistance R as a function of V_{TG} and V_{BG} measured at $T = 300$ mK for device S1 with $\theta = 1.8°$. **b** R as a function of n at $D/\epsilon_0 = 0$. The peaks corresponding to the CNP and full fillings of the bands ($\pm n_s$) in the dual-gated region are marked for clarity. **c** High-resolution map showing the R as a function of D and n near the CNP. **d** R as a function of D at $n = 0$ showing the insulator-semimetal-insulator transition. **e** Schematic illustration of the band structure of TDTLG at three different electric fields. The gap closes at a finite electric field D_0/ϵ_0 ~0.1 V/nm and opens again as the D is increased further.

intrinsic single-particle gaps at the CNP and insulating states at $\pm n_s$. Meanwhile, the insulator-semimetal-insulator transition is observed in all devices (Supplementary Figs. 2, 4) and, thus, is intrinsic to TDTLG.

The electric field tunable electronic states, especially the intrinsic gap state in TDTLG, is interesting from a fundamental point of view. To gain further insight into the intrinsic gap state of TDTLG, we measured the differential conductance (dI/dV) at $T = 255$ mK as a function of source-drain bias V_{Bias} and V_{BG} at three fixed V_{TG} (marked with three dashed lines in Fig. 2a), as shown in Fig. 3a–c. We find that the differential conductance map for $V_{TG} = 0.16$ V (Fig. 3a) reveals a large diamond-like structure centered at the CNP. The line cut of dI/dV at $D/\epsilon_0 = 0$ as a function of V_{Bias} is plotted in Fig. 3d (blue color). For $V_{Bias} < 3$ mV, dI/dV remains close to 0, while it rises sharply when V_{Bias} is increased further to 5 mV, and finally shows a linear increase with further increment of V_{Bias}. This "U" shape feature demonstrates the presence of an intrinsic bandgap in TDTLG.

Next, the stability diagram for $V_{TG} = 0.4$ V (Fig. 3b) shows a much smaller diamond-like structure centered at the CNP. The corresponding dI/dV curve at the center of the diamond (or at $D/\epsilon_0 = 0.05$ V/nm) (yellow color

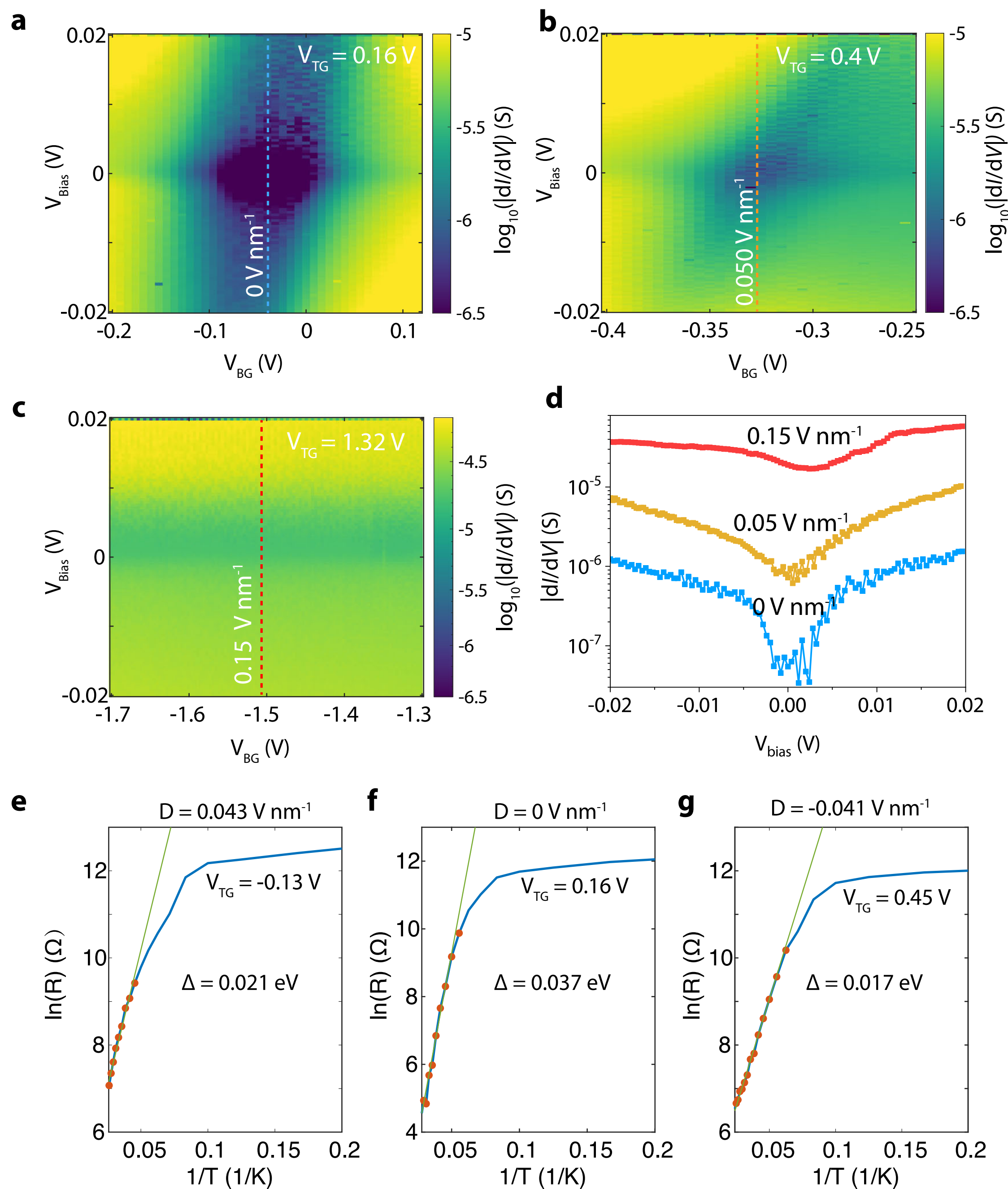

Fig. 3 | Differential conductance and temperature dependence of resistance. **a–c** Differential conductance dI/dV of the device S1 as a function of V_{Bias} and V_{BG} at a fixed top gate voltage of 0.16, 0.4, and 1.32 V, respectively (marked in Fig. 2a). The device exhibits diamond-like structure for $V_{TG} = 0.16$ V, which almost vanishes at $V_{TG} = 1.32$ V, suggesting the closing of the bandgap. **d** dI/dV as a function of V_{Bias} for three different values of D, marked by dashed lines in (**a**–**c**). **e**–**g** Arrhenius plots presenting the T-dependence of resistance recorded at three different values of D. The solid lines show the Arrhenius-like fits to the data, where Δ is the extracted bandgap of the device.

in Fig. 3d) presents a "V" shape feature, revealing a smaller gap at $D/\epsilon_0 = 0.05$ V/nm than the gap at $D/\epsilon_0 = 0$. Finally, no diamond-like structure is seen for the stability diagram measured at $D/\epsilon_0 = 0.15$ V/nm, and the dI/dV is predominantly independent of bias (as shown in the corresponding dI/dV curve in Fig. 3d) and gate, suggesting the gap closes at a larger D field of $D/\epsilon_0 = 0.15$ V/nm.

Temperature dependence

To further quantify the magnitude of intrinsic bandgap in TDTLG, we performed a detailed study of the temperature dependence of the resistance. Figure 3e–g show Arrhenius plots of the temperature dependence of resistance at the CNP for the dual-gated region at three different values of the D/ϵ_0 field (0.043, 0, and −0.041 V/nm). In all three cases, the experimental data above 15−20 K follow the behavior expected for thermally-activated transport, according to $R = R_0 \exp(\Delta/2k_BT)$, where k_B is the Boltzmann constant and R_0 and Δ are fitting parameters. A maximum energy gap Δ = 37 meV is extracted for $D/\epsilon_0 = 0$ V/nm, and two reduced energy gaps Δ = 21 meV for $D/\epsilon_0 = 0.043$ V/nm and Δ = 17 meV for $D/\epsilon_0 = -0.041$ V/nm. At lower values of T, the deviation from the thermally-activated behavior to a much weaker T-dependence can be attributed to a combination of the Mott variable-range hopping conduction mediated by localized states and quantum tunneling through a short-

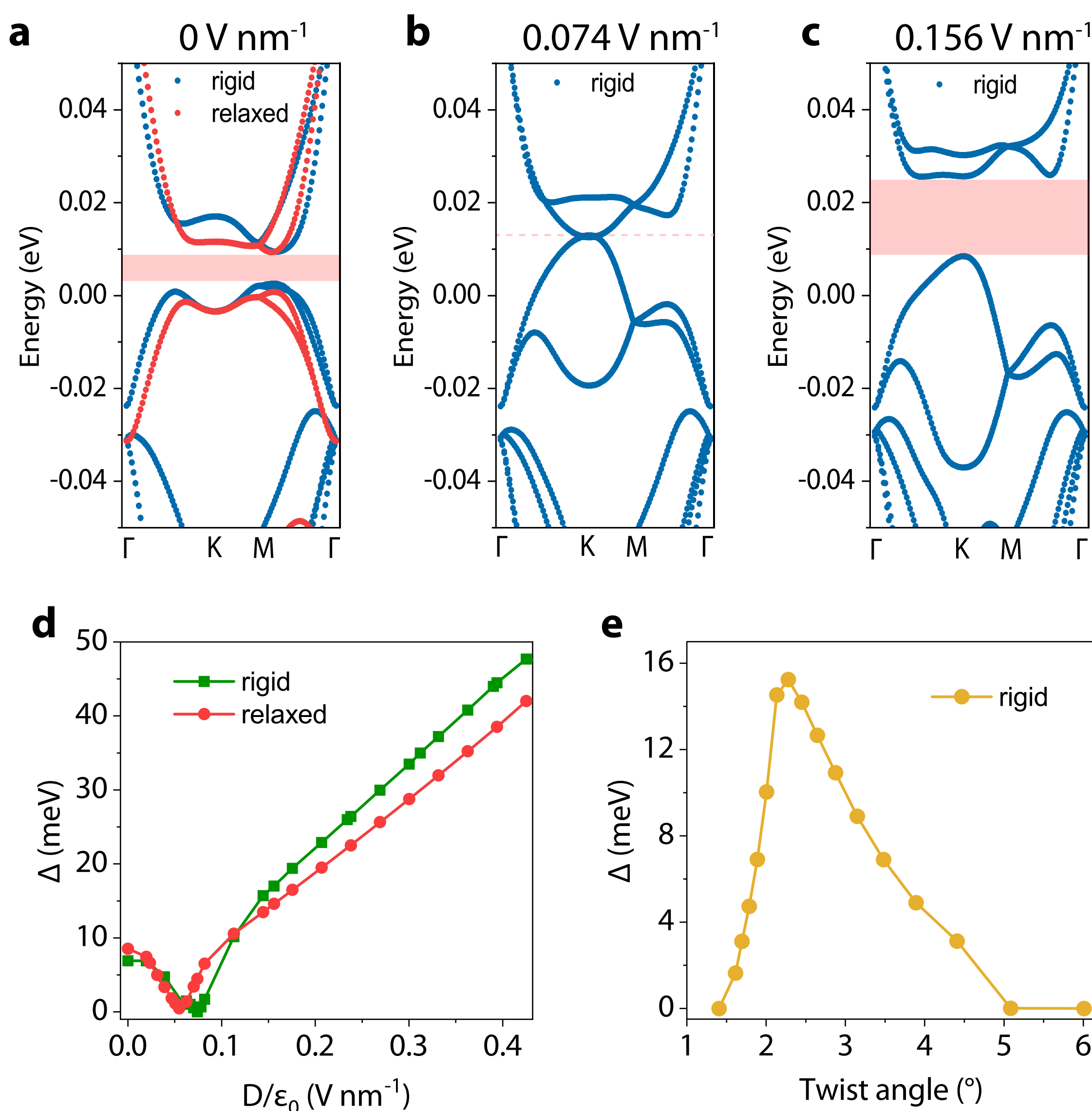

Fig. 4 | Theoretical calculations. a Calculated band structure of ABC-ABC stacked TDTLG with $\theta = 1.8^{\circ}$ in the absence of an external electric field. The blue (orange) lines denote the bands of an unrelaxed (relaxed) TDTLG. **b**, **c** Calculated band structure in the presence of an external field. The displacement field D has been calculated using the dielectric constant of h-BN and screening effects have been ignored. **d** Bandgap as a function of D for both the relaxed (red curve) and unrelaxed (green curve) structure of ABC-ABC stacked TDTLG. **e** Bandgap as a function of twist angle for unrelaxed ABC-ABC stacked TDTLG in the absence of an external displacement field.

channel semiconductor[29]. We note that the insulating state near the CNP survives up to temperatures as high as 40 K. (Supplementary Fig. 3). In an additional device S4 (Supplementary Fig. 4), we measure the T-dependence of resistance over a wide range of D fields. At CNP and large D fields, the device behaves like an insulator as the resistance decreases as T goes up, which agrees well with the literature ref. 30. At the critical field $D = D_0$=0.21 V/nm, the resistance first slightly decreases and then increases after T drops down to a critical point (10 K), suggesting a semimetal behavior[31,32]. A detailed discussion on device S4 can be found in Supplementary Fig. 4.

Theoretical calculation

Finally, we have performed tight-binding calculations to rationalize the observed charge-transport behavior and get insights into the band structure. The band structures of TDTLG as a function of twist angles and displacement field were calculated using the tight-binding model implemented in WannierTools[33]. The tight-binding Hamiltonian was built using orbital distance-dependent Slater–Koster parameters and considers second-nearest-neighbor interactions. For the relaxed band structures, the atomic positions of TDTLG were relaxed using the classical force field approximation implemented in LAMMPS[34]. The ABC-CAB domains display the largest out-of-plane relaxation of atomic positions, while the ABC-ABC domains have the least (Supplementary Fig. 5). This behavior minimizes the repulsion between "C-C" regions at the twisted layer.

Figure 4a shows the band structure of unrelaxed (blue) and relaxed (orange) ABC-ABC stacked TDTLG at a twist angle of $\theta = 1.8^{\circ}$. The calculations show that TDTLG is intrinsically an insulator—with a bandgap of ~0.01 eV, as observed experimentally in Fig. 2a. The intrinsic bandgap at the CNP may be attributed to the absence of inversion symmetry in twisted ABC-ABC stacked TDTLG. This behavior is similar to that reported for TDBLG for the same twist angle[35]. A comparison of the unrelaxed/rigid and relaxed bands shows that lattice relaxation has a negligible effect on the band structure around the Fermi energy, again similar to that reported for TDBLG[35].

Figure 4a–c show the closing and reopening of the bandgap with increasing displacement field, indicating an insulator-semimetal-insulator transition, consistent with our experimental observation. This is in contrast with the behavior of twisted ABA-ABA stacked graphene, which is an intrinsic insulator in the absence of an external field, becomes metallic in the presence of low external fields, but does not revert to insulating behavior upon a further increase of the external field (Supplementary Fig. 6). However, as illustrated in ref. 26, the device can exhibit several stacking configurations. To correlate the charge-transport behavior with stacking configuration, we have performed the calculations on Thirty-two sliding configurations, as discussed in ref. 26 (Supplementary Fig. 7). We find that there are eight configurations that exhibits a variation in the bandgap similar to ABC-ABC stacking. In all other configurations, the system either remains semimetallic or shows a very small bandgap upon crossing a critical displacement field. Based on the symmetry arguments, we can narrow down the possible configurations in our devices to ABC-ABC, CAB-ABC, CAB-ACB, and CBA-BCA (see Supplementary Information for discussion). Further, as demonstrated in ref. 26, CAB-ABC/BCA-BCA are energetically the least favorable configurations with respect to the configuration with no sliding and are therefore unlikely to exist in our devices. Additionally, theoretical calculations show that CAB-ACB, and CBA-BCA have large stacking energy[26], but it is impossible to rule out these possibilities as stacking energy data are not available for all configurations. In conclusion, while the ABC-ABC stacking configuration is more likely to exist in our devices, CAB-ACB, CAB-ABC, or CBA-BCA configurations, or a combination thereof, may also exist.

Further, a comparison of Fig. 4b, c to Fig. 4a shows that the presence of a displacement field leads to a splitting in the valence bands, as well as the conduction bands. The position and dispersion of valence bands below -0.02 eV remain largely unaffected by the external field, while the increased dispersion and splitting of both the degenerate conduction and valence bands around 0 eV lead to the closing of the bandgap at displacement fields around 0.074 V/nm, as observed in panel Fig. 4b. A similar behavior has been reported in TDBLG[35] and was attributed to layer polarization and correlation effects. It was demonstrated that the displacement field in the $+z$ direction leads to an asymmetry in the layer contribution to the bands around the Fermi energy in TDBLG. The valence bands become confined within the top layer, while the conduction bands become confined to the bottom layer. In addition to layer polarization, there is an enhancement in the density of states in the conduction bands around the Fermi energy. This makes the correlation effects stronger in the conduction bands than in the valence bands, leading to an electron-hole asymmetry in the external fields.

As shown in Fig. 4d, lattice relaxation has a negligible effect on the overall trend of the bandgap as a function of the displacement field. Both the unrelaxed and relaxed ABC-ABC stacked TDTLG are intrinsic insulators in the absence of an external displacement field. An insulator-to-semimetal transition is observed for a displacement field slightly below 0.1 V/nm, and a semimetal-to-insulator transition is observed for a displacement field slightly above 0.1 V/nm. The bandgap increases monotonically for $D/\epsilon_0 > 0.1$ V/nm. The displacement fields required to observe insulator-metal-insulator transitions are slightly lower than that those observed experimentally. We attribute this to the absence of screening effects in the tight-binding model[36].

Figure 4e shows the bandgap of ABC-ABC stacked TDTLG as a function of twist angle in the absence of an external displacement field. Without a twist, the system has no bandgap and behaves like an ABC-stacked trilayer graphene[37]. The bandgap increases with twist angle to a maximum around $\theta \approx 2.5^{\circ}$ and then decreases for larger twist angles. We speculate that this non-monotonic behavior originates from an interplay between the reduced coupling in some regions of the trilayer-trilayer interface and the periodicity of those regions due to angle-induced lattice mismatch.

Conclusions

In summary, we have performed the first electrical measurements on twisted double trilayer graphene for small twist angle devices (~1.7−2.0°). Our measurements show the presence of an intrinsic bandgap in this heterostructure, which is supported by tight-binding calculations. In addition, we also observe an insulator-semimetal-insulator transition, which results from the closing and reopening of the bandgap upon an increase of the displacement field. The presence of an intrinsic bandgap in TDTLG opens up the possibility of exploiting such devices for optoelectronic applications[38], in particular, because its size is highly tunable by the applied displacement field. Moreover, we anticipate that further tuning of devices with twist angle closer to ~1.2−1.5° will lead to stronger correlation effects and, in turn, symmetry-broken many-body phases.

Methods

Device fabrication

The TDTLG devices were fabricated following a typical "tear and stack" technique[27,28]. Trilayer graphene, h-BN (20−35 nm thick) and graphite flakes were mechanically exfoliated on SiO_2/Si (100 nm oxide thickness). The heterostructure was assembled using standard dry-transfer techniques[39]. We used poly bisphenol A carbonate (PC) supported by polydimethylsiloxane (PDMS) on a glass slide to first pick up h-BN and then tear and pick up the trilayer graphene. A commercial micromanipulator was used to control the rotation angle. The graphite flake was finally picked up as a bottom gate. The fabrication of the metal top gate and electrodes followed a standard electron-beam lithography process and electron-beam metal evaporation. The devices were designed into a four-terminal structure shaped by traditional reactive ion etching with a CHF_3 and O_2 gas mixture. Finally, all the contacts were shaped as 1D edge contacts with Cr/Au electrodes[39].

Electronic measurements

Transport measurements were performed in a He_3 cryostat with a base temperature of 255 mK. We applied standard lock-in techniques to measure the resistance, with 17.777 Hz excitation frequency and 1 nA excitation current. Although the devices had four contacts, they were not patterned in a four-terminal Hall-bar or van der Pauw geometry for accurate four-terminal measurements. Hence, we conducted measurements in a two-terminal configuration to avoid artifacts that can arise from a "pseudo" four-terminal geometry.

Twist angle extraction

To estimate the twist angle, we used the relation $n_s = 8\theta^2/\sqrt{3}a^2$ (including valley and spin degeneracies), where $a = 0.246$ nm is the lattice constant of graphene and n_s is the charge carrier density corresponding to a fully filled superlattice unit cell[1].

Band structure calculations

Tight-Binding Model Calculations—The tight-binding model Hamiltonian for carbon atoms in WannierTools considers only the p_z orbitals.

$$H = \sum_{ij} \varepsilon_i a_i^{\dagger} a_j + \sum_{i \neq j} V_{ij} a_i^{\dagger} a_j \tag{1}$$

with $\varepsilon_i = E_{z_i}$, where E is the strength of the electric field, z_i is the atomic z-axis coordinate, and $a_i^{\dagger}$ and a_j are the creation and annihilation operators.

$$V_{ij} = V_{pp\pi} \sin^2\theta + V_{pp\sigma} \cos^2\theta \tag{2}$$

where $V_{pp\sigma}$ and $V_{pp\pi}$ are σ-type and π-type Slater–Koster parameters, θ is the angle between the orbital axes and $R_{ij} = R_i - R_j$ connecting the two orbital centers. The Slater–Koster parameters depend on the distance r between two orbitals as

$$V_{pp\pi}(r) = V^0_{pp\pi} e^{q_\pi (1 - \frac{r}{a_\pi})} F_c(r) \tag{3}$$

$$V_{pp\sigma}(r) = V^0_{pp\sigma} e^{q_\sigma (1 - \frac{r}{a_\sigma})} F_c(r) \tag{4}$$

where a_π is the first nearest neighbor distance in the plane, a_σ is the interlayer distance, and $V^0_{pp\pi}$ and $V^0_{pp\sigma}$ are the corresponding coupling values. The smooth cutoff function that takes into account the distance between orbitals is given by

$$F_c(r) = \left(1 + e^{\frac{r-r_c}{l_c}}\right)^{-1} = \left\{\begin{matrix} 1 & r \ll r_c \\ 0 & r \gg r_c \end{matrix}\right\} \quad (5)$$

The on-site energy of p_z orbitals is set to $\epsilon_i = -0.78$ eV to adjust the reference. The following constants have been used in the above equations; $V^0_{pp\pi} = -2.81$ eV, $V^0_{pp\sigma} = 0.48$ eV, $q_\sigma = 7.428$, $a_\pi = 1.418$ Å, $q_\pi = 3.1451$, $l_c = 0.265$ Å, $a_\sigma = 3.5$ Å, and $r_c = 6.165$ Å[36,40].

Classical Force—Field Simulations—The second generation REBO potential[41] and the Kolmogorov- Crespi potential[42] were used to describe the intralayer and interlayer interactions respectively in the lattice relaxation of TDTLG in LAMMPS. The relaxation was performed until the total force acting on each atom was less than 10^{-6} eV/atom using the FIRE algorithm[43].

Data availability

The datasets generated during and/or analyzed during the current study are available from the authors on reasonable request.

Received: 28 June 2023; Accepted: 8 February 2024;
Published online: 27 February 2024

References

1. Cao, Y. et al. Correlated insulator behaviour at half-filling in magic-angle graphene superlattices. *Nature* **556**, 80 (2018).
2. Cao, Y. et al. Unconventional superconductivity in magic-angle graphene superlattices. *Nature* **556**, 43 (2018).
3. Chen, G. et al. Signatures of tunable superconductivity in a trilayer graphene moiré superlattice. *Nature* **572**, 215–219 (2019).
4. Chen, G. et al. Evidence of a gate-tunable mott insulator in a trilayer graphene moiré superlattice. *Nat. Phys.* **15**, 237–241 (2019).
5. Shen, C. et al. Correlated states in twisted double bilayer graphene. *Nat. Phys.* **16**, 520–525 (2020).
6. Liu, X. et al. Tunable spin-polarized correlated states in twisted double bilayer graphene. *Nature* **583**, 221–225 (2020).
7. Cao, Y. et al. Tunable correlated states and spin-polarized phases in twisted bilayer–bilayer graphene. *Nature* **583**, 215–220 (2020).
8. Chen, S. et al. Electrically tunable correlated and topological states in twisted monolayer-bilayer graphene. *Nat. Phys.* **17**, 374–380 (2021).
9. Xu, S. et al. Tunable van hove singularities and correlated states in twisted monolayer–bilayer graphene. *Nat. Phys.* **17**, 619–626 (2021).
10. Park, J. M., Cao, Y., Watanabe, K., Taniguchi, T. & Jarillo-Herrero, P. Tunable strongly coupled superconductivity in magic-angle twisted trilayer graphene. *Nature* **590**, 249–255 (2021).
11. Hao, Z. et al. Electric field-tunable superconductivity in alternating-twist magic-angle trilayer graphene. *Science* **371**, 1133–1138 (2021).
12. Park, J. M. et al. Robust superconductivity in magic-angle multilayer graphene family. *Nat. Mater.* **21**, 877–883 (2022).
13. Wang, L. et al. Correlated electronic phases in twisted bilayer transition metal dichalcogenides. *Nat. Mater.* **19**, 861–866 (2020).
14. Zhang, Z. et al. Flat bands in twisted bilayer transition metal dichalcogenides. *Nat. Phys.* **16**, 1093–1096 (2020).
15. Lu, X. et al. Superconductors, orbital magnets and correlated states in magic-angle bilayer graphene. *Nature* **574**, 653–657 (2019).
16. Serlin, M. et al. Intrinsic quantized anomalous hall effect in a moiré heterostructure. *Science* **367**, 900–903 (2020).
17. Sharpe, A. L. et al. Emergent ferromagnetism near three-quarters filling in twisted bilayer graphene. *Science* **365**, 605–608 (2019).
18. Bhowmik, S. et al. Spin-orbit coupling-enhanced valley ordering of malleable bands in twisted bilayer graphene on wse2. *Nat. Commun.* **14**, 4055 (2023).
19. Ghiotto, A. et al. Quantum criticality in twisted transition metal dichalcogenides. *Nature* **597**, 345–349 (2021).
20. Ghawri, B. et al. Breakdown of semiclassical description of thermoelectricity in near-magic angle twisted bilayer graphene. *Nat. Commun.* **13**, 1522 (2022).
21. Regan, E. C. et al. Mott and generalized wigner crystal states in wse2/ws2 moiré superlattices. *Nature* **579**, 359–363 (2020).
22. Li, H. et al. Imaging two-dimensional generalized wigner crystals. *Nature* **597**, 650–654 (2021).
23. Zhang, F., Sahu, B., Min, H. & MacDonald, A. H. Band structure of a b c-stacked graphene trilayers. *Phys. Rev. B* **82**, 035409 (2010).
24. Zhou, H. et al. Half-and quarter-metals in rhombohedral trilayer graphene. *Nature* **598**, 429–433 (2021).
25. Zhou, H., Xie, T., Taniguchi, T., Watanabe, K. & Young, A. F. Superconductivity in rhombohedral trilayer graphene. *Nature* **598**, 434–438 (2021).
26. Halbertal, D. et al. Unconventional non-local relaxation dynamics in a twisted trilayer graphene moiré superlattice. *Nat. Commun.* **13**, 7587 (2022).
27. Kim, K. et al. van der waals heterostructures with high accuracy rotational alignment. *Nano Lett.* **16**, 1989–1995 (2016).
28. Cao, Y. et al. Superlattice-induced insulating states and valley-protected orbits in twisted bilayer graphene. *Phys. Rev. Lett.* **117**, 116804 (2016).
29. Khodkov, T., Khrapach, I., Craciun, M. F. & Russo, S. Direct observation of a gate tunable band gap in electrical transport in abc-trilayer graphene. *Nano Lett.* **15**, 4429–4433 (2015).
30. Dean, C. R. et al. Boron nitride substrates for high-quality graphene electronics. *Nat. Nanotechnol.* **5**, 722–726 (2010).
31. Scherwitzl, R. et al. Metal-insulator transition in ultrathin lanio 3 films. *Phys. Rev. Lett.* **106**, 246403 (2011).
32. Yang, W. et al. Hofstadter butterfly and many-body effects in epitaxial graphene superlattice. *Nano Lett.* **16**, 2387–2392 (2016).
33. Wu, Q., Zhang, S., Song, H.-F., Troyer, M. & Soluyanov, A. A. Wanniertools: an open-source software package for novel topological materials. *Comput. Phys. Commun.* **224**, 405–416 (2018).
34. Thompson, A. P. et al. Lammps-a flexible simulation tool for particle-based materials modeling at the atomic, meso, and continuum scales. *Comput. Phys. Commun.* **271**, 108171 (2022).
35. Choi, Y. W. & Choi, H. J. Intrinsic band gap and electrically tunable flat bands in twisted double bilayer graphene. *Phys. Rev. B* **100**, 201402 (2019).
36. Haddadi, F., Wu, Q., Kruchkov, A. J. & Yazyev, O. V. Moiré flat bands in twisted double bilayer graphene. *Nano Lett.* **20**, 2410–2415 (2020).
37. Lui, C. H., Li, Z., Mak, K. F., Cappelluti, E. & Heinz, T. F. Observation of an electrically tunable band gap in trilayer graphene. *Nat. Phys.* **7**, 944–947 (2011).
38. Deng, B. et al. Strong mid-infrared photoresponse in small-twist-angle bilayer graphene. *Nat. Photon.* **14**, 549–553 (2020).
39. Wang, L. et al. One-dimensional electrical contact to a two-dimensional material. *Science* **342**, 614–617 (2013).
40. De Laissardiere, G. T., Mayou, D. & Magaud, L. Numerical studies of confined states in rotated bilayers of graphene. *Phys. Rev. B* **86**, 125413 (2012).
41. Brenner, D. W. et al. A second-generation reactive empirical bond order (rebo) potential energy expression for hydrocarbons. *J. Phys. Condens. Matter* **14**, 783 (2002).
42. Kolmogorov, A. N. & Crespi, V. H. Registry-dependent interlayer potential for graphitic systems. *Phys. Rev. B* **71**, 235415 (2005).
43. Bitzek, E., Koskinen, P., Gähler, F., Moseler, M. & Gumbsch, P. Structural relaxation made simple. *Phys. Rev. Lett.* **97**, 170201 (2006).

Acknowledgements

J.Z. acknowledges support from the Empa Directorate under the Empa Internal Research Call 2021. M.C. acknowledges support from the Swiss National Science Foundation under the Sinergia grant no. 189924

(Hydronics) and the EC H2020 FET Open project no. 767187 (QuIET). M.L.P. acknowledges funding from the Eccellenza Professorial Fellowship no. PCEFP2_203663, as well as supported by the Swiss State Secretariat for Education, Research and Innovation (SERI) under contract number MB22.00076. A.J. acknowledges support by the NCCR MARVEL, a National Center of Competence in Research, funded by the Swiss National Science Foundation (grant number 205602). K.W. and T.T. acknowledge support from the JSPS KAKENHI (Grant Numbers 19H05790 and 20H00354). The authors thank the Cleanroom Operations Team of the Binnig and Rohrer Nanotechnology Center (BRNC) for their help and support.

Author contributions

J.Z. conceived and designed the experiments. J.Z. fabricated the devices and performed the Raman measurements. J.Z. and M.L.P. performed the electrical measurements. K.W. and T.T. provided h-BN crystals. J.Z. and M.L.P. analyzed the data. A.J., under the supervision of D.P., did the theoretical calculations. B.G., J.Z., M.L.P., and M.C. discussed the figures and wrote the manuscript. All authors discussed the results and their implications and commented on the manuscript. M.L.P., A.J., and B.G. contributed equally to this work.

Competing interests

The authors declare no competing interests.

Additional information

Supplementary information The online version contains supplementary material available at https://doi.org/10.1038/s41699-024-00449-w.

Correspondence and requests for materials should be addressed to Mickael L. Perrin, Michel Calame or Jian Zhang.

Reprints and permissions information is available at http://www.nature.com/reprints

Publisher's note Springer Nature remains neutral with regard to jurisdictional claims in published maps and institutional affiliations.

Open Access This article is licensed under a Creative Commons Attribution 4.0 International License, which permits use, sharing, adaptation, distribution and reproduction in any medium or format, as long as you give appropriate credit to the original author(s) and the source, provide a link to the Creative Commons licence, and indicate if changes were made. The images or other third party material in this article are included in the article's Creative Commons licence, unless indicated otherwise in a credit line to the material. If material is not included in the article's Creative Commons licence and your intended use is not permitted by statutory regulation or exceeds the permitted use, you will need to obtain permission directly from the copyright holder. To view a copy of this licence, visit http://creativecommons.org/licenses/by/4.0/.

© The Author(s) 2024